This is the peer reviewed version of the following article: Ficek M., Dec B., Sankaran K. J., Gajewski K., Tatarczak P., Wlasny I., Wysmolek A., Haenen K., Gotszalk T., Bogdanowicz R., Stable Field Electron Emission and Plasma Illumination from Boron and Nitrogen Co-Doped Edge-Rich Diamond-Enhanced Carbon Nanowalls, Advanced Materials Interfaces,Vol. 8, iss. 20 (2021), 2100464, which has been published in final form at https://doi.org/10.1002/admi.202100464. This article may be used for non-commercial purposes in accordance with Wiley Terms and Conditions for Use of Self-Archived Versions. This article may not be enhanced, enriched or otherwise transformed into a derivative work, without express permission from Wiley or by statutory rights under applicable legislation. Copyright notices must not be removed, obscured or modified. The article must be linked to Wiley's version of record on Wiley Online Library and any embedding, framing or otherwise making available the article or pages thereof by third parties from platforms, services and websites other than Wiley Online Library must be prohibited.

Stable field electron emission and plasma illumination from boron and nitrogen co-doped edge-rich diamond-enhanced carbon nanowalls

Mateusz Ficek[1], Bartłomiej Dec[1], Kamatchi Jothiramalingam Sankaran[2], Krzysztof Gajewski[3], Piotr Tatarczak[4], Igor Wlasny[4], Andrzej Wysmolek[4], Ken Haenen[5,6], Teodor Gotszalk[3] and Robert Bogdanowicz[1]*

[1] Department of Metrology and Optoelectronics, Faculty of Electronics, Telecommunications, and Informatics, Gdańsk University of Technology, 11/12 Narutowicza St., 80-233 Gdańsk (Poland)

[2] CSIR-Institute of Minerals and Materials Technology, Bhubaneswar, Odisha-751013, India. [3] Division of Nanometrology Wrocław University of Science and Technology, Faculty of Microsystem Electronics and Photonics, ul. Z. Janiszewskiego 11/17, PL-50372 Wrocław, Poland

[4] Institute of Experimental Physics, Faculty of Physics, University of Warsaw, Pasteura 5, 02-093 Warsaw, Poland

[5] Institute for Materials Research (IMO), Hasselt University, 3590 Diepenbeek, Belgium

[6] IMOMEC, IMEC vzw, 3590 Diepenbeek, Belgium.

[*]Corresponding author**:** *rbogdan@eti.pg.edu.pl* (R. Bogdanowicz).

Keywords: Edge-rich Diamond/Graphene Nanostructures, Cross-Sectional Analysis, Kelvin Probe Force Microscopy, *Ab-Initio* Simulations, Electron Field Emission.

Abstract: Superior field electron emission characteristics were achieved in edge-rich diamond-enhanced carbon nanowalls (D-ECNWs) grown in a single-step chemical vapor deposition process co-doped with boron and nitrogen. The structure consists of sharp, highly conductive graphene edges supplied by a solid, diamond-rich bottom. The Raman and transmission electron microscopy studies revealed a hybrid nature of sp^3-diamond and sp^2-graphene in these nanowalls. Nanoscopic atomic force microscopy studies displayed more conduction sites at the surface of the nanowalls. Kelvin probe force microscopy also revealed the work function of these nanowalls is 4.75 eV. The *ab-initio* calculations also carried out that support the experimental observations of diamond-graphene hybrid model. Finally, this hybrid D-ECNWs was employed as a cathode in a field electron emission (FEE) device resulting in a low turn-on field of 3.1 V/μm, a large field enhancement factor, a high FEE J_e of 2.6 mA/cm^{2,} and long lifetime stability of 438 min. Such an enhancement in the FEE originates from the unique materials combination, resulting in good electron transport from the graphene phases and efficient FEE of electrons from the sharp edges on the nanowalls. The prospective application

of these materials is displayed by employing these hybrids as cathodes in a microplasma device ensuing a low threshold voltage of 160 V and high plasma stability of 140 min, which confirms the role of these hybrid structured nanowalls in the enhancement of electron emission.

1. Introduction

Over the last few years, carbon nanowalls (CNW) [1–3] grown by chemical vapor deposition have gained great popularity mainly due to their high surface area and high field electron emission (FEE). Such CNWs are compared to graphene nanosheets, grown vertically to the substrate [4]. Recent studies of low-dimensional materials such as graphene and nanodiamond show excellent charge transfer at the main plain and edges even with structural imperfections such as surface defects [5]. Nevertheless, carbon nanomaterials such as nanotubes, nanoflakes, or even graphene have been used as extraordinary electron sources [6]. Their FEE characteristics are superior [7], but they show poor stability and a short lifetime [8], which prevents them from becoming a practical material for device applications. Basically, the FEE process involves two steps including the electron transporting into the emitting sites and the electron tunneling into vacuum from the effective emitting sites under a typical electric field. The overall FEE performance could be influenced by the electrically conducting pathways and the effective emitting sites [9,10].

The mentioned materials, despite having many attractive properties, are outgrown by boron-doped nanowalls (B-CNWs). B-CNWs have excellent additional properties such as tunable band gap, high conductivity [11], excellent mechanical resistivity [12], and high optical absorbance [13]. Thanks to those properties, it was possible to report the successful use of B-CNWs for electrochemical detection [14,15]. Also, Zhou *et al.* [16] used B-CNWs for a highly sensitive pressure sensor, and Haining *et al.* [17] showed that microstructural modification shows enhanced electron field emission. Moreover, thanks to their graphene-like structure, they show great potential as a material for supercapacitors due to their high surface area [2,4]. The subject of B-CNWs is highly popular and they are being used for building biosensors [14], resistive switching memory devices [18], perovskite solar cells [19], and electron emission devices [20].

Despite their interesting properties, growing these nanowalls was quite a complicated process but it was done previously by Hiramatsu *et al.* [21] using coupled radiofrequency and plasma-enhanced CVD. Moreover, Wu *et al.* [22] reported the successful growth of CNWs on catalyzed substrates using microwave plasma-assisted CVD. Furthermore, one of the latest

MOST WIEDZY Downloaded from mostwiedzy.pl

reports by Sankaran *et al.* [20] shows the successful growth of CNWs with plasma-assisted CVD. Sobaszek *et al.* [23] proposed the growth mechanism of B-CNWs. They concluded that such type of B-CNWs is a p-type semiconductor structure with high hole-acceptor concentration (up to 3.33×10^{23} cm^{-3}). Recently, Zhai *et al.* showed that post-growth treatment of nanocarbons in a hydrogen plasma improves FEE, decreasing the turn-on potential and increasing the emission current density thanks to the transformation of sp^2-bonded CNWs to sp^3-bonded diamond [22]. Nevertheless, the plasma bombardment during H_2 plasma treatment may cause severe damage to the nanostructured carbon materials, could hinder the practical application.

This study is intended to investigate the origin of novel diamond-enhanced carbon nanowall (D-ECNW) nanostructures in a single-step chemical vapor deposition process and their superior FEE characteristics. The morphology and microstructure of D-ECNW are investigated using scanning electron microscopy and high-resolution transmission electron microscopy (with electron energy loss spectroscopy). Depth profile Raman mapping studies reveal the phase changes in the material. Nanoscopic cross-sectional atomic force microscopy studies are carried out to determine the localized emission sites and work function of the materials. In addition, experimental results are supported by *ab-initio* analysis using density functional theory (DFT) methods. The potential application of these superior FEE D-ECNW nanostructures as microplasma cathodic devices is also demonstrated.

2. Experimental

D-ECNWs were synthesized on a p-type (100) Si wafer using a microwave plasma-enhanced chemical vapor deposition system (SEKI Technotron AX5400S, Japan) with details described elsewhere [24]. The substrate's temperature was kept constant at 700°C during the deposition process. Excited plasma was ignited by microwave radiation (2.45 GHz) with a microwave power of 1300 W. The base pressure was about 10^{-6} Torr, while the process pressure was kept at 50 Torr. The source gas mixture of $H_2/CH_4/N_2$ at gas volume 325 sccm of total flow rate was applied. Moreover, the doping level of boron in the gas phase expressed as the [B]/[C] ratio, was kept at 2000 ppm using diborane (B_2H_6) as a dopant precursor. The D-ECNWs were grown for 6 h to reach a thickness of ~3 μm. The surface morphology and the microstructure of these materials were examined with a SEM (Phenom XL) and transmission electron microscopy (Jeol 2100F), and an EELS (Gatan Enfina) in TEM, respectively.

The Raman spectroscopy measurements were performed using a Horiba Jobin Yvon T64000 spectrometer working in a single grating setup, equipped with an automated 3-axis

MOST WIEDZY Downloaded from mostwiedzy.pl

stage with 100 nm spatial resolution. As an excitation source, a Kimmon Koha He-Cd dual-mode (325 nm/422 nm) laser was used. The 422 and satellite lines were removed with a series of optical filters. The laser light with a power of 23 mW was focused on the sample with an Olympus MPFLN50x objective with 50× magnification. This setup allowed for the acquisition of wide-range spectra in both single points and as maps with a sub-micron lateral scale. The analysis of the Raman spectra was conducted in the dedicated Phyton-based software.

AFM measurements were performed using a Veeco/Bruker Nanoman V with a Nanoscope V controller working in conductive atomic force microscopy (C-AFM) and Kelvin probe force microscopy (KPFM) modes. In order to measure the current flow from the sample to the scanning tip in C-AFM mode, a logarithmic trans-impedance amplifier was mounted in the microscope. The typical sample bias was 0.1 V. Nanosensors PPP-ContPt probes with a spring constant of 0.2 N/m, a resonant frequency of 13 kHz and a $PtIr_5$ coating were used in the experiments. To retrieve the current, recorded data were processed taking into account the calibration curve. During the C-AFM experiments, the surface of the nanowalls was imaged.

In KPFM mode, each scan line was passed twice. In the first scan, the topography signal of the sample was recorded. During the second scan, the contact potential difference (CPD) between the sample and the scanning tip was measured. Nanosensors PPP-EFM probes with a spring constant of 2.8 N/m, resonant frequency of 75 kHz, and a $PtIr_5$ coating were used. The typical electrical oscillation amplitude was 1200 mV. The probe was lifted up 50 nm above the sample during the KPFM scan. The work function of the investigated sample was estimated based on the calibration measurement of a material with a known work function (WF). In the present study, it was highly–oriented pyrolytic graphite (HOPG, WF ~4.6 eV) [25]. During the KPFM experiments, the cross-section view, showing the area of the nanowalls and substrate, was imaged. Furthermore, samples were freshly cut before the experiment and ground.

The density functional theory simulations were conducted with the Quantum ATK [26] software from Synopsys. The geometry optimization was achieved with an integrated molecular dynamics package: ATK-ForceField calculator (ATK-FF) [27], employing ReaxFF potential [28]. Calculated models reach accuracy better than 0.01 eV/ Å of force and 0.01 eV/$Å^3$ of stress error. The optimized structures were applied for the calculation of the electronic properties utilizing the density functional based on the tight-binding (DFTB) method [29]. The self-consistent Slater–Koster tight-binding model was supplied by matsci-0-3 semi-relativistic potentials [30]. The designed D-ECNW structure was configured as a one-electrode system [31], containing 1682

MOST WIEDZY Downloaded from mostwiedzy.pl

atoms in total. The specific atomic ratio of boron and nitrogen dopants to carbons was applied following prior X-ray photoelectron spectroscopy (XPS) results reported by Sankaran *et al.* [20].

The FEE characteristics of the D-ECNW nanostructures were measured using a tunable parallel-plate setup [32]. In the FEE measuring setup, the cathode-to-anode distance was controlled by a micrometer. The current−voltage (I−V) characteristics were measured under a pressure of 10^{-6} Torr using an electrometer (Keithley 2410). The FEE behavior of the diamond films was extracted from the I−V curves using the Fowler−Nordheim (F−N) model [33],

$$J_e = \left[\frac{AB^2\beta^2}{\emptyset}\right] \exp\left[-\frac{B\emptyset^{3/2}}{\beta E}\right] \quad (1)$$

where J_e is the FEE current density, A = 1.54 × 10^{-6} eV/V^2 and B = 6.83 × 109 $eV^{-3/2}$ V/m, β is the field-enhancement factor, E is the applied field, and φ is the work function of the electron field emitting materials. The turn-on field (E_0) for the FEE process is designated as the point of intersection of the straight lines extrapolated from the low- and high-field segments of the F−N plots, namely, *ln* (J_e/E^2) versus 1/E curves [33].

The plasma illumination (PI) characteristics of the D-ECNW nanostructures were also examined. The microplasma device consisted of an anode of indium tin oxide (ITO) coated glass and D-ECNW nanostructures as a cathode [32]. The cathode-to-anode separation was fixed by a 1.0 mm thick Teflon spacer. A cylindrical microcavity was formed by creating a 3.0 mm diameter circular hole in the Teflon spacer. The whole device was placed in a vacuum chamber, maintaining a base pressure of 0.01 mTorr. A DC pulsed voltage under 2 Torr of Ar (10 sccm) was used to ignite the microplasma. Using a Keithley 2410 electrometer, we acquired the plasma current density (J_{PI}) versus applied field (E) characteristics. Moreover, through ITO-coated glass, the plasma was viewed by a USB microscope and plasma photographs were recorded for different applied voltages to illustrate the PI characteristic of the microplasma device.

3. Results and discussion

3.1. Material's characteristics

The growth process of D-ECNWs requires H^+, H_yCNH_x, BH_x, CH^+_x, and C_2 species in the plasma [11], which are essential for the formation of the nanowall-like configuration [23,34]. The formerly reported growth of CNWs, nanosheets, or nanoneedles was assigned only to CN molecules [35]. The D-ECNW morphology, shown in the SEM images (see Figure 1a), implies that the structure grows anisotropically in the N_2/CH_4 plasma. Sankaran *et al.* [36] revealed that

MOST WIEDZY Downloaded from mostwiedzy.pl

the growth rates along the longitudinal and circumferential directions differ significantly from those of the needle-like to circular grains.

The high-resolution SEM micrograph of the D-ECNW shown in Figure 1a reveals the dense and straight morphological nanowalls of lengths around 0.5–3 μm and few nanometers in thickness. The thickness of the nanowalls is around 2.28–3.20 μm with sharp edges at the top of the nanowalls (Figure 1b). These features are homogeneously distributed all over the film surface. The deposited nanowalls of these samples are nearly straight, which is a different outcome than the maze-like CNWs reported by others [37,38].

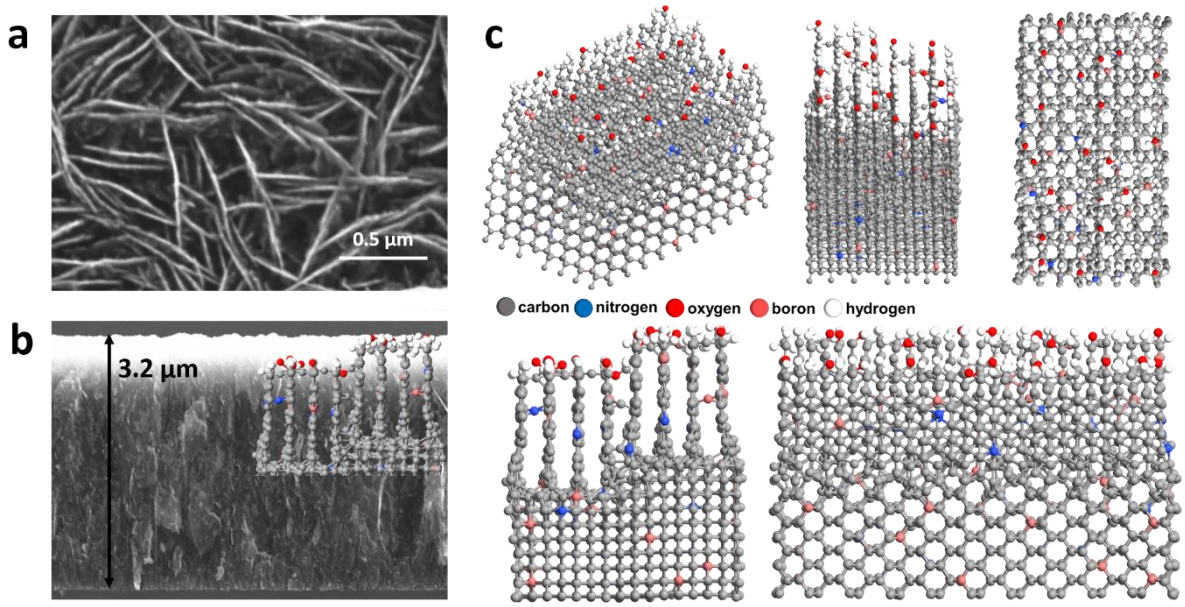

Figure 1. (a) Plan-view and (b) cross-sectional view SEM micrographs of D-ECNW along with (c) proposed atomic structure including 5 different views: 3D view (top-left and top-middle), XY-view (top-right), XZ view (bottom-left) and YZ view (bottom-right).

In-depth Raman studies were carried out to investigate the crystalline quality of the D-ECNWs. Two types of measurements were conducted in Raman spectroscopy to estimate the structure of the grown material entirely – the experiment consisted of two-dimensional Raman mapping of the surface and linear mapping of the material's cross-section. In the former case, the Raman spectra were acquired over a square grid consisting of 225 points, spanning a square-shaped area with x and y sides length of 105 μm.

MOST WIEDZY Downloaded from mostwiedzy.pl

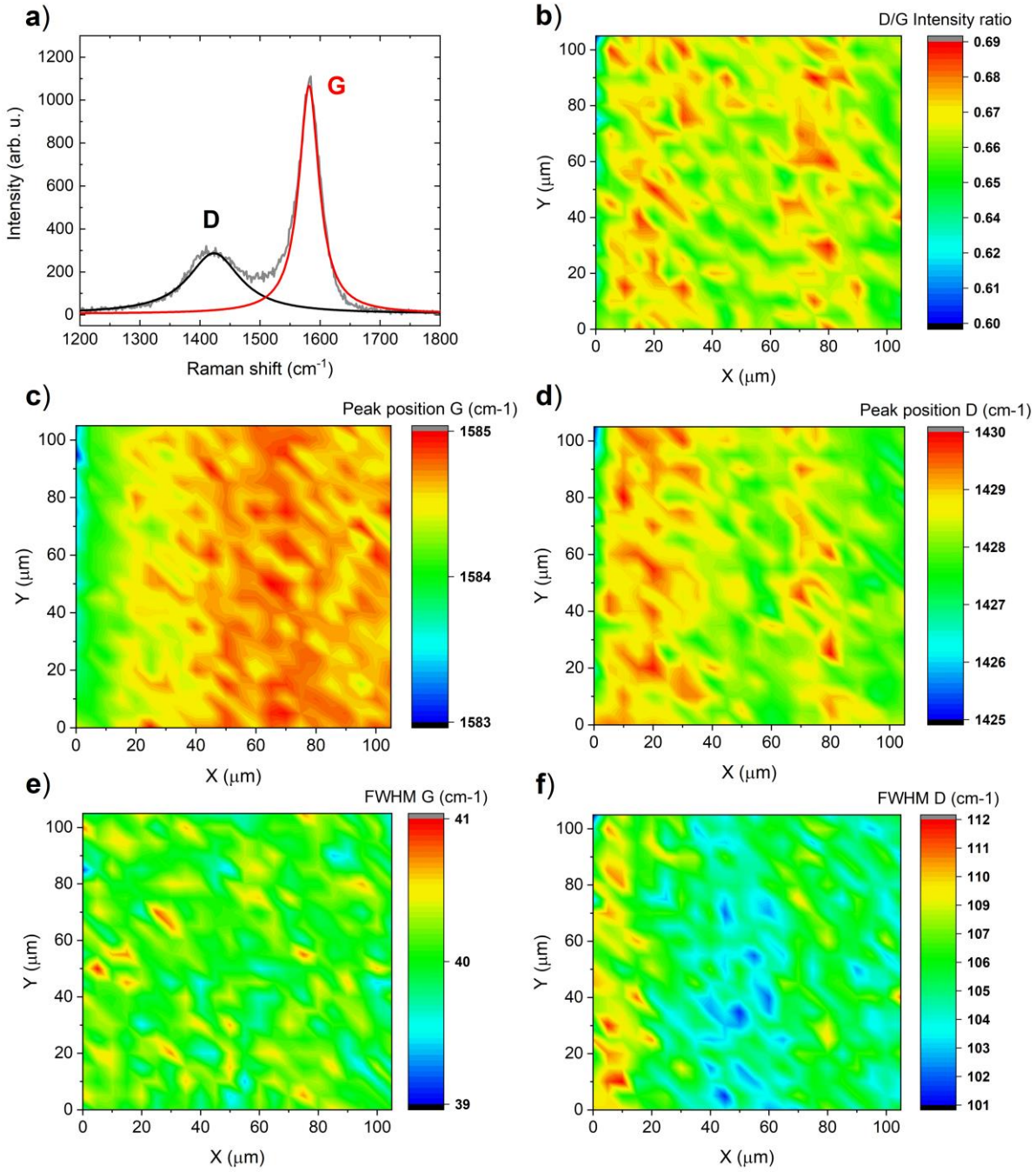

Figure 2. Raman spectrum of the D-ECNW sample with Lorentzian curves fitted to both D and G spectral lines of the material (a); Raman maps of (b) D to G intensity ratio, (c) G line position, (d) D line position, (e) G line width and (f) D line width.

Subsequently, the spectra were analyzed concerning the carbon content of the sample, thus the focus was put on the vicinity of the D and G bands associated with the vibrational modes of carbon structures. The exemplary Raman spectrum of the area is shown in Figure 2a. Two intensive lines can be found. The first one is located at about 1426 cm^{-1}. Considering that a 325 nm laser was used in the experiment, this line can be assigned to the D band of the sp^2

MOST WIEDZY Downloaded from mostwiedzy.pl

hybridized carbon structures [39]. Its presence is related to both the defects in the sp^2 carbon material and the boundaries of the grains or sheets of the material [40]. The intensity of this line is expected to be high, considering that the graphene-like sheets are oriented perpendicularly to the surface of the sample and, therefore, their edges are located on the immediate surface of the sample. The second line, located at about 1584 cm^{-1}, can be identified as the G band of sp^2 carbon [39] related to the stretching of the C-C bonds [40]. It is noteworthy that no other lines are present, including those related to the sp^3 carbon hybridization, which indicates that the material is, indeed, well defined.

The distribution of the structure throughout the sample surface is quite uniform, as evidenced by a low variation of the D to G line intensities, as shown in Figure 2b. The mean value of this parameter is equal to 0.66 with a standard deviation of only 0.01, albeit sites with a ratio over 0.8 can also be found. These would indicate larger defect sites created during or post-growth. Our results, however, lead us to believe that there are no significant differences in the flake size of the carbon nanowalls, based on the fact that the ratio of the Raman signal of the whole sample surfaces does not show signs of significant variation. Similar uniformity can be found in the strain of the nanowalls. The assessment of this parameter was conducted based on the position of the G line within the spectrum, as a correlation between the position of the G band and the mechanical strain of the sp^2 carbon is a well-known fact [41,42]. This parameter also shows little variation, as shown in Figure 2c. Furthermore, the value of the position of both G and D lines (see Figure 2cd) is close to that of the as-grown CVD single sp^2 carbon layers [39], albeit this is to be expected, since the layers grow vertically and, thus, interact little with the substrate, particularly at a certain height.

The last parameter analyzed based on the Raman spectra is the sub-micron scale uniformity or disorder of the strain, which is related to the width of the spectral lines. The maps of the widths of G and D lines are seen in Figure 2ef. In both cases, sites with significantly higher width values show some correlation with a high D/G intensity ratio. This may be explained by a greater number of smaller nanowall flakes in those areas. Due to their smaller sizes and stochastic distribution of strain, a higher defect density in this area cannot be excluded.

MOST WIEDZY Downloaded from mostwiedzy.pl

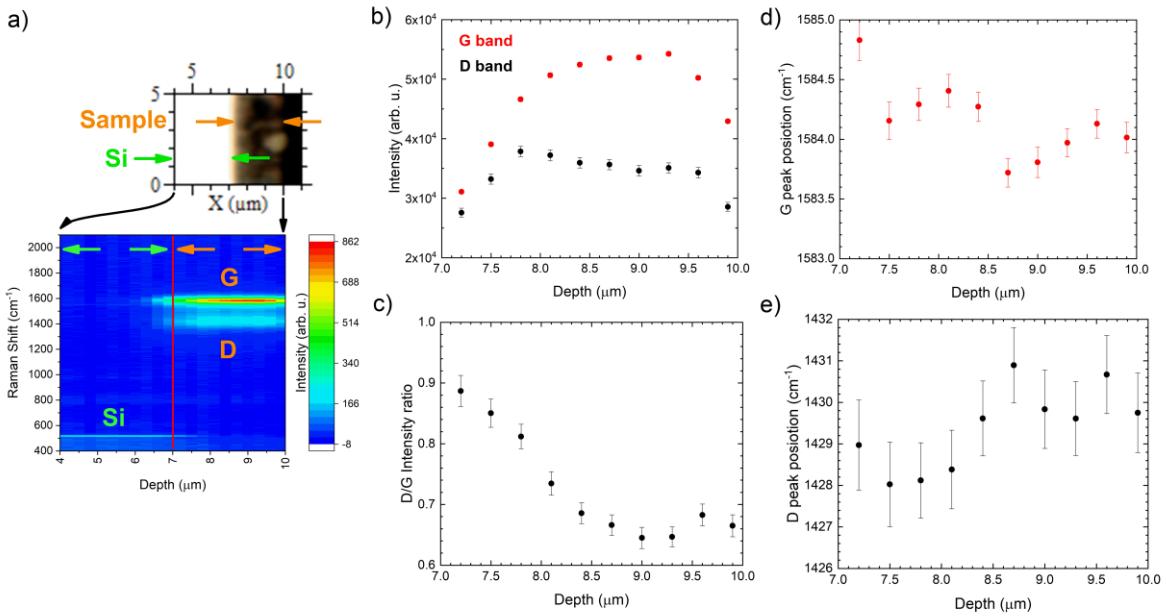

Figure 3. Optical image and depth profile of D and G Raman lines of the D-ECNW sample cross-section (a); Depth profiles of G and D band intensity (b); D to G intensity ratio (c); G band position and (d) D line position (e).

The results of the depth profiling based on the Raman investigations of the D-ECNW sample cross-section shed more light on the structure of the grown layers. This experiment was performed on the edge of a cleaved sample and reveals significant differences at various depths in relation to the immediate surface of the material (Figure 3a), albeit the changes seem to be continuous, rather than sudden, showing a clear indication of a correlation between the height of the grown material, and thus the separation of the surface and the substrate, and its properties.

The intensities of the G and D lines show some variation close to the surface and in the vicinity of the interface with the Si substrate (Figure 3b). However, this variation results from the finite laser spot size on the sample, which is observed for the Si phonon signal which is smoothly changing while crossing the interface with the substrate. Much more valuable information can be obtained from the analysis of the D to G intensity ratio (Figure 3c), which shows a significant increase close to the substrate (see Figure 3c). Therefore, one can expect that while the material is packed more densely since the fragments of the nanowalls are also smaller, the contribution of edges into the Raman signal is higher. This model is consistent with the analysis of the position of the G line, as shown in Figure 3d. The position of the G line slightly decreases by about 1 cm^{-1} between the immediate surface of the sample and the nanowall-substrate interface. The shifting of the G line is associated with an increase of strain of the material [40,41]. This strain is most likely correlated with a higher density of the material

MOST WIEDZY Downloaded from mostwiedzy.pl

grown in the initial phases of the process. More information could be obtained from the analysis of the D line position (Figure 3e), apparently, it is much broader than G line and no firm conclusions could be made.

The microstructure and the bonding characteristics of the D-ECNWs were investigated using TEM with EELS. The plan-view bright field (BF) TEM micrograph shown in Figure 4a illustrates the evolution of nanostructures with the branching features representing an anisotropic grain growth. The selective area electron diffraction (SAED) pattern (inset of Figure 4a), corresponding to the BF-TEM, contains diffraction rings representing the (111), (220), and (311) diamond lattices, and the presence of sp^2-bonded carbon in this hybrid is indicated by a very bright diffuse ring at the center of the SAED pattern. Figure 4b shows the high-resolution TEM (HRTEM) micrograph of the D-ECNWs corresponding to the region "A" and Figure 4a, indicating the diamond grains are encapsulated by graphene grain boundaries. The graphene layers of thickness ranging from a few atomic layers to more than 10 layers. The Fourier transformed (FT) images (insets 1, 2, and 3) confirm the presence of diamond in region "1" at edges and graphene in regions "2" and "3", respectively.

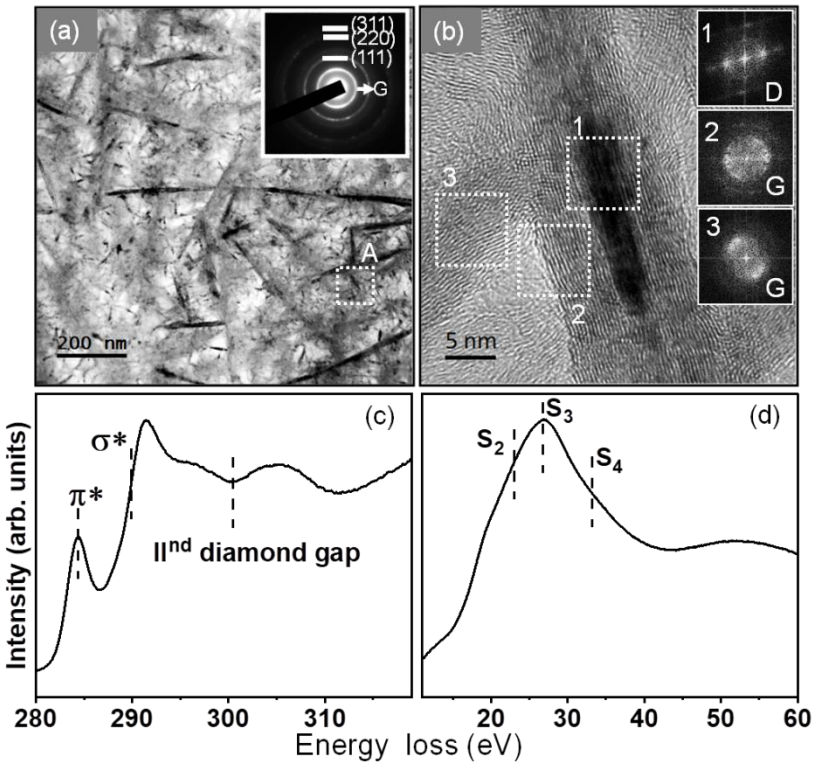

Figure 4. (a) A plan-view bright-field TEM (BF-TEM) image of the D-ECNWs, whereas the corresponding SAED pattern, is shown as an inset. (b) The high-resolution TEM image, the structure image, was obtained for the region marked as "A" in a. The FT diffractogram images, 1-3, shown in the insets of b of the corresponding regions "1-3" represent the existence of diamond and graphite phases, respectively. (c) The core-loss and (d) the plasmon loss EELS spectra of the D-ECNWs corresponding to BF-TEM image in a.

MOST WIEDZY Downloaded from mostwiedzy.pl

To investigate the various carbon phases in the D-ECNWs, the carbon K-edge EELS in TEM was carried out. Figure 4c shows the core-loss EELS spectrum of the D-ECNWs, which indicates that the D-ECNWs have both sp^3-bonded carbon (i.e., diamond), signified by a rise at 289 eV (σ*-band) and a dip in the vicinity of 302 eV (second diamond gap)[45], and by a π*-band at 285 eV indicates sp^2-bonded carbon [46]. To categorize between graphite and amorphous carbon phases, the plasmon-loss EELS measurements in TEM were also carried out. The plasmon-loss EELS spectrum of the D-ECNWs shown in Figure 4d discloses a peak near 33 eV (S_4) along with a shoulder near 23 eV (S_2) designate diamond phases and a peak around 27 eV (S_3) confirms the graphitic phase in the D-ECNWs [47]. TEM and EELS investigations in Figure 4 evident that the D-ECNWs contain a hybrid structure of nanosized diamond grains and well-crystallized nano-graphitic phases.

Based on the material's characteristics, Figure 1c displays the proposed atomic structure of D-ECNW taken into consideration the recently revealed multi-step growth mechanism [48], which was in agreement with prior conclusions demonstrated in [34] and [37]. The D-ECNW possesses a hybrid structure with two in-depth sections: (I) rigid boron and nitrogen co-doped diamond and (II) maze-like boron and nitrogen co-doped diamond-graphene nanowalls. The base boron and nitrogen co-doped diamond section (I) originates from the efficient CH_3 bonding at the HCN-rich sites re-forming graphite-rich structure into a diamond lattice. Nevertheless, this process is depth-limited until the growth is not de-generated by a large amount of HCN defects induced by CN_x species competing with CH_3. Yiming et al. [38] reported on the major H abstraction by nitrogen species disintegrating the standard chemistry of diamond growth in section (I) and facilitating the pathway for the formation of HCN defects. This results in the growth of section (II) of the boron and nitrogen co-doped diamond-graphene section. The specific depth of the boron-doped diamond section (I) could also be ascribed to the fact that the nanodiamonds seeding the surface have limited influence on the re-nucleation process in the latter phases of the growth but contribute efficiently to the sp^3-rich structure just at the initial stages of the growth.

Later, the chemistry is overtaken by covalent adsorbing of CN_x molecules inducing slight nitrogen doping (as revealed by XPS in [24]) simultaneously with boron incorporation attributed to the large concentrations of BH_x radicals in the gas phase. BH_x species are particularly responsible for re-nucleation processes extending the length of the nanowall surfaces in section (II) allowing also for the synthesis of nanocrystalline diamond inclusions/clusters [49] splitting the walls into dendrite-like structures. The diamond-graphene

MOST WIEDZY Downloaded from mostwiedzy.pl

nanowall re-nucleation is also induced constantly thanks to the C_2 species favoring the formation of ultra-small diamond grains [50].

3.2 Nanoscopic investigation of electronic properties of D-ECNW

Figures 5a and 5b displayed the topography and conductivity map of the D-ECNWs recorded in C-AFM mode, respectively. The topography image seems to be consistent with the SEM micrograph (Figure 1a). A slight increase in the size of single D-ECNW detail is related to the measurement method and scanning tip used for C-AFM imaging. The maximum height difference observed in the image was 296.6 nm with an average roughness of 41.7 nm. The D-ECNW was densely packed and no exact direction arrangement of D-ECNW growth can be observed. The AFM measurement (inset) indicated a typical thickness of a single D-ECNW to be below 100 nm.

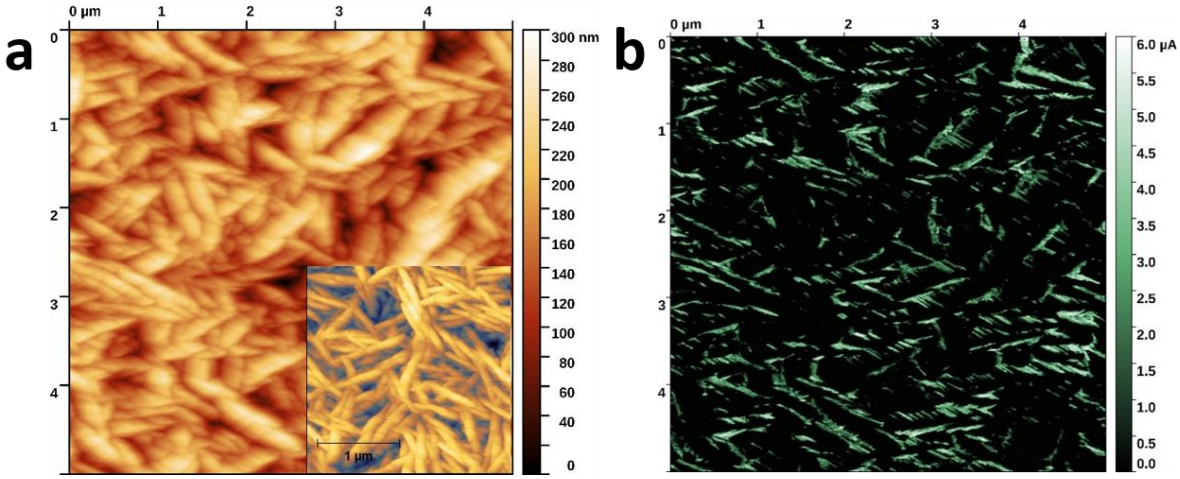

Figure 5. Top-view of the D-ECNW surface: (attn. logarithmic I/V converter); (b) C-AFM cantilever (attn. current logarithmic I/V converter) images.

The conductivity map shows strong non-uniformity of current flowing through the sample. The high conduction regions are concentrated on the edges of the D-ECNW. This could be an effect of exposed graphene areas, observed in Raman and TEM studies (see Figures 2-4), showing metallic contact between the sample and the tip. The maximum recorded current was 6.15 µA. Taking into account sample bias, the obtained value is a local indicator of high D-ECNW conductivity. It should be noted that previous studies reported much smaller current values [51–53].

Figure 6 displays the KPFM results obtained at the D-ECNW surface as follows: the optical picture of the sample (Figure 6a), topography (Figure 6b), CPD (Figure 6c), phase signal

MOST WIEDZY Downloaded from mostwiedzy.pl

(Figure 6d), and sectional view of the topography and CPD (Figure 6f). The surface of a freshly cut sample is very flat with a typical roughness of 11.4 nm in the area of the substrate.

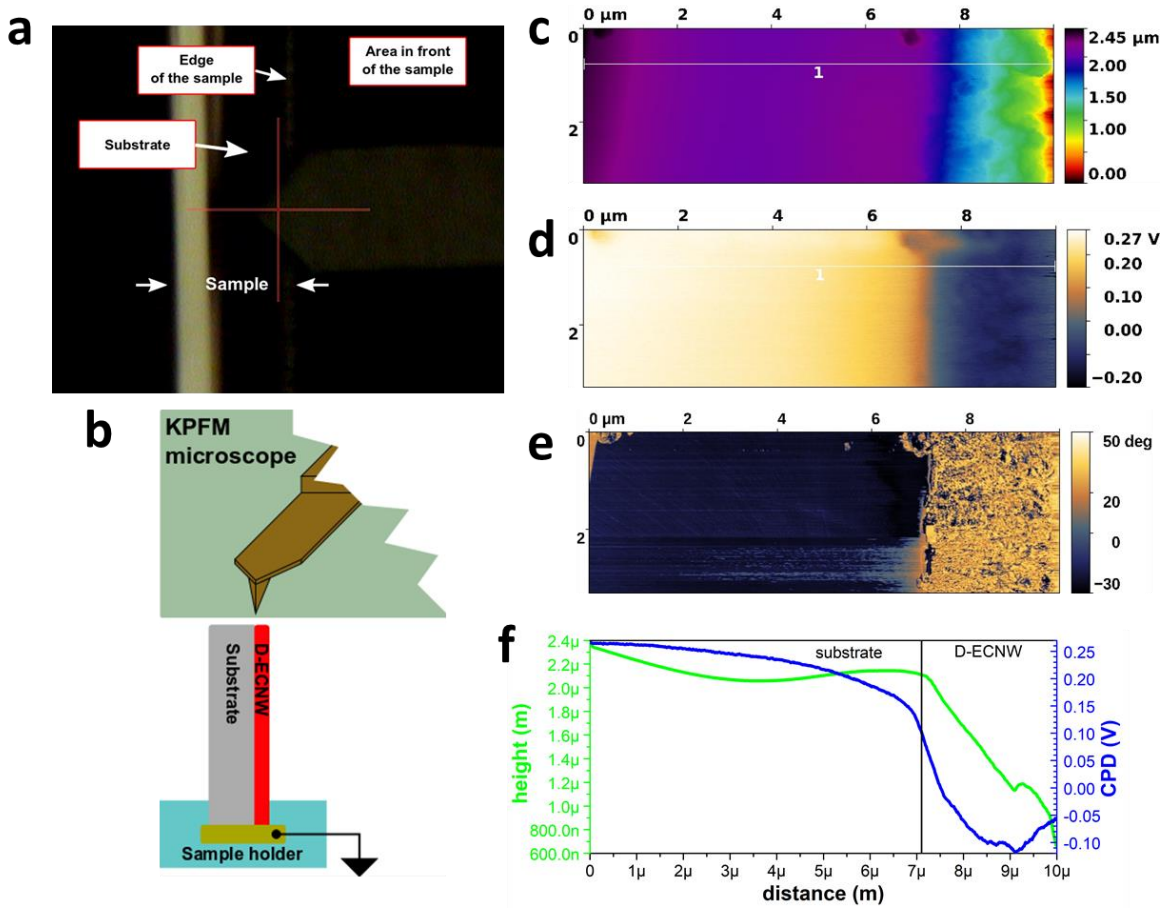

Figure 6. KPFM studies at the cross-section of D-ECNW: (a) Optical view of the imaged sample; (b) Schematic view of the cross-section KPFM imaging; (c) Topography; (d) CPD; (e) Phase signal; (f) Sectional view on the topography and CPD.

In the area of D-ECNW, the roughness increased up to 43.7 nm. The material difference between the substrate and the D-ECNW can be clearly distinguished on the CPD and phase images. It suggests the D-ECNW height is approximately 3 µm. The estimated work function of the substrate was 4.65 eV and D-ECNW was 4.95 eV. The CPD gradient between the top and bottom parts of the D-ECNW was approximately 0.07 V/µm. Thus, the obtained results are consistent with the recent works [42,43].

3.3. Ab-initio study of electronic properties of D-ECNW structures

The D-ECNW was simulated using a slab as displayed in the flat surface representation in Figure 7a. The Projected Local Density of States (PLDOS) showed conduction and valence band locations at simulated D-ECNW structure (see Figure 7b). The D-ECNW slab can be

MOST WIEDZY Downloaded from mostwiedzy.pl

divided into two main sections. The first is the boron and nitrogen co-doped diamond section ((I) in Figure 7ab, Z in 0–5 Å range), which shows high valence band occupation energy due to boron doping. The interface region (5–6 Å) shows high energy density not only at the valence band but also at the conduction band due to boron doping and sp^2-sp^3 carbon bonding. The second region is the boron and nitrogen co-doped graphitic nanowalls, which start from 6 Å length in the Z direction ((II) in Figure 7ab). Such characteristics of Partial-DOS were previously reported by Palash *et al.* [56], where the obtained results showed band gap relocation dependent on the dopant type in the graphene sheet. Moreover, the work of Gholizadeh and Yang-Xin [57] confirms a shift of the band gap with co-doped graphene sheets.

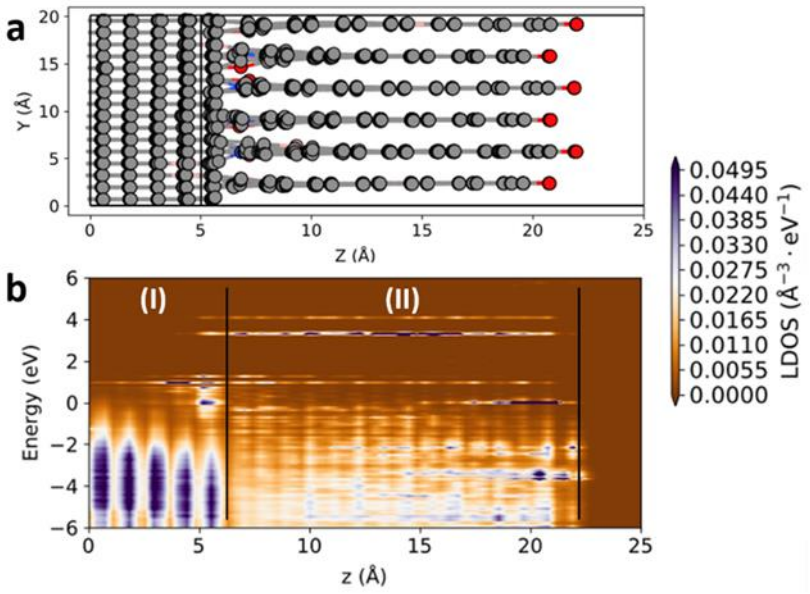

Figure. 7. *Ab-initio* simulations of D-ECNW structure; (a) Cross-sectional view of D-ECNW atomic structure; (b) Projected Local Device Density of States of D-ECNW atomic model. The gray color is Carbon, blue – Nitrogen, red – Oxygen, Pink – Boron.

Section (I) of D-ECNW structure (see Figure 7ab) exhibits a DFTB-calculated band gap of 5.79 eV, which is slightly larger than experimental data (5.47 eV) [58] and similar with the other simulations 5.78 eV [59]. The applied in the paper DFTB method typically overestimates the diamond band gap, while the DFT method results in the underestimated band gap of 4.19 eV as manifested by Shen et al. [60]. Due to the large size of the slab, we have chosen DFTB method because it is much faster and results in a less significant discrepancy in comparison with the experimental studies of the diamond band gap. Moreover, the boron and nitrogen co-doped graphitic nanowalls (section II) showed a band gap of approx. 0.15eV, which corresponds with values presented by Sharma et al. reporting a 0.3 eV gap for boron-doped graphene [61]. Closer

MOST WIEDZY Downloaded from mostwiedzy.pl

to the first section edge, nitrogen doping is higher where we can see its presence at the conduction band. Moreover, the oxygen provides an additional increase in the PLDOS plot at the valence band at -3.66 eV (see Figure 7b).

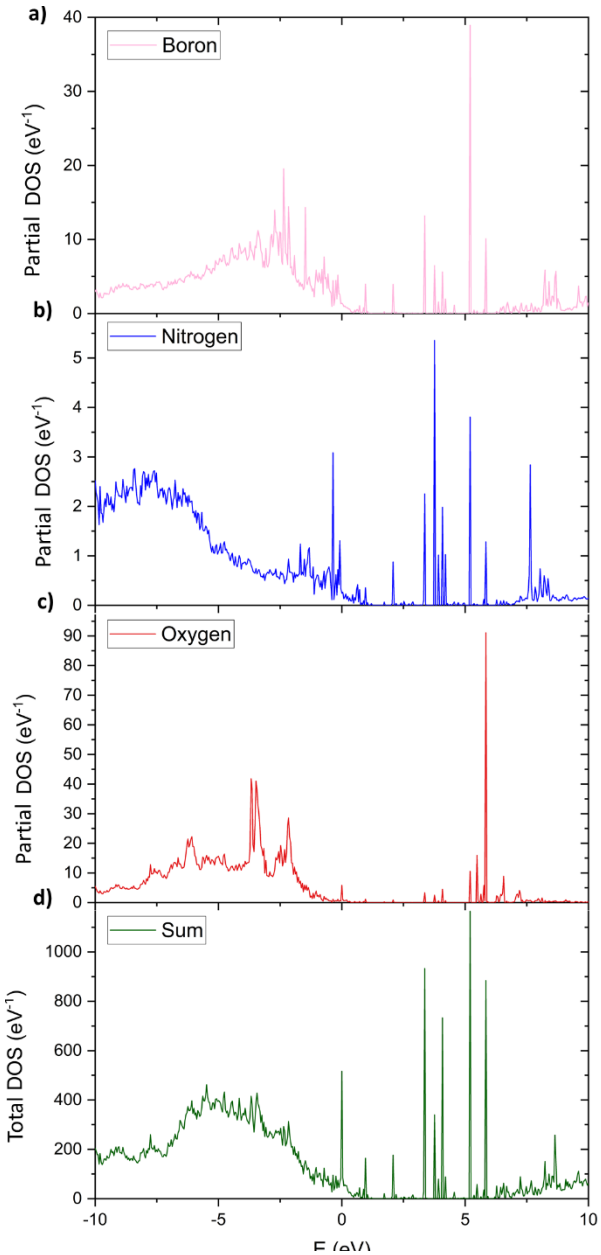

Figure. 8. *Ab-initio* simulations of Density of States of D-ECNW structure; (a) Partial DOS of Boron atoms; (b) Partial DOS of Nitrogen atoms; (c) Partial DOS of Oxygen atoms; (d) Total DOS of D-ECNW slab shown in Figure 7.

The density of states (DOS) of the whole slab (see Figure 8) shows the final electronic character of the D-ECNW structure. The total band gap of the D-ECNW structure was estimated as 1.15 eV, which corresponds to the results of Palash *et al.* (up to 1.2 eV of band gap)[56]. The Partial Density of States (Partial-DOS) showed that oxygen does not influence the band gap

MOST WIEDZY Downloaded from mostwiedzy.pl

(see Figure 8c), but generally has approx. 10% impact on the Total DOS (see Figure 8d). The Nitrogen presented in Figure 8b closes the gap but overall exhibits a minor impact on the Total DOS (less than 1%). The Boron displayed in Figure 8a reveals a relatively moderate effect on the Total DOS performance (~5%) but introduces distinctive peaks which influence the final band gap.

3.4. Field electron emission studies of diamond-enhanced carbon nanowalls

The excellent electronic characteristics of these D-CNW hybrid nanostructures lead to enhanced FEE characteristics as shown in Figure 9a. The D-ECNW nanostructures display a low E_0 value of 3.1 V/μm and a high J_e of 2.6 mA/cm^2 at an applied field of 5.5 V/μm. The slope of the F-N plot (Figure 9b) provides a large β value of 3875 for the D-ECNW nanostructures. Moreover, the FEE lifetime stability of the D-ECNW nanostructures (inset of Figure 9a) reveals 438 min estimated at a J_e value of 1.19 mA/cm^2, which corresponds to a working field of 5.15 V/μm. Remarkably, the D-ECNW nanostructures exhibit much lower turn-on potential than recently reported in the literature for hydrogen-treated carbon nanowalls/diamond samples (E_0 = 4.3 V μm^{-1}[22]). Next, it should be noted that the FEE measurements were reproducible at various regions on a similar sample, representing that the FEE behavior is very uniform over the D-ECNW nanostructures.

Now the question to be answered is, what is/are the factor(s) responsible for the efficient FEE characteristics of these D-ECNWs. It is observed from Raman and TEM studies, the D-ECNWs contain a hybrid nature of sp^3-diamond grains encased in sp^2-graphitic grain boundaries. The SEM micrographs reveal the presence of sharp edges at the top of the nanowalls. It is revealed from C-AFM studies there is a presence of conduction regions on the edges of the D-ECNW. The graphene phases encasing the diamond grains are responsible for these conduction regions. The FEE mechanism is proposed based on the above observations as follows: as the sp^2 graphene phase increased the percolative conduction paths in the D-ECNWs [51,52], the numerous sharp edges on the top of the nanowalls induced a fast electron transport rate [9,10,62–66], thus resulting in enhanced FEE characteristics viz. low E_0, large β and high J_e values. Moreover, the presence of sp^3-diamond grains assisted in achieving a high FEE lifetime stability of these nanowalls. The D-ECNW nanostructures with efficient FEE characteristics are suitable as a cathode material for microplasma-based cathodic devices, which will be discussed shortly.

MOST WIEDZY Downloaded from mostwiedzy.pl

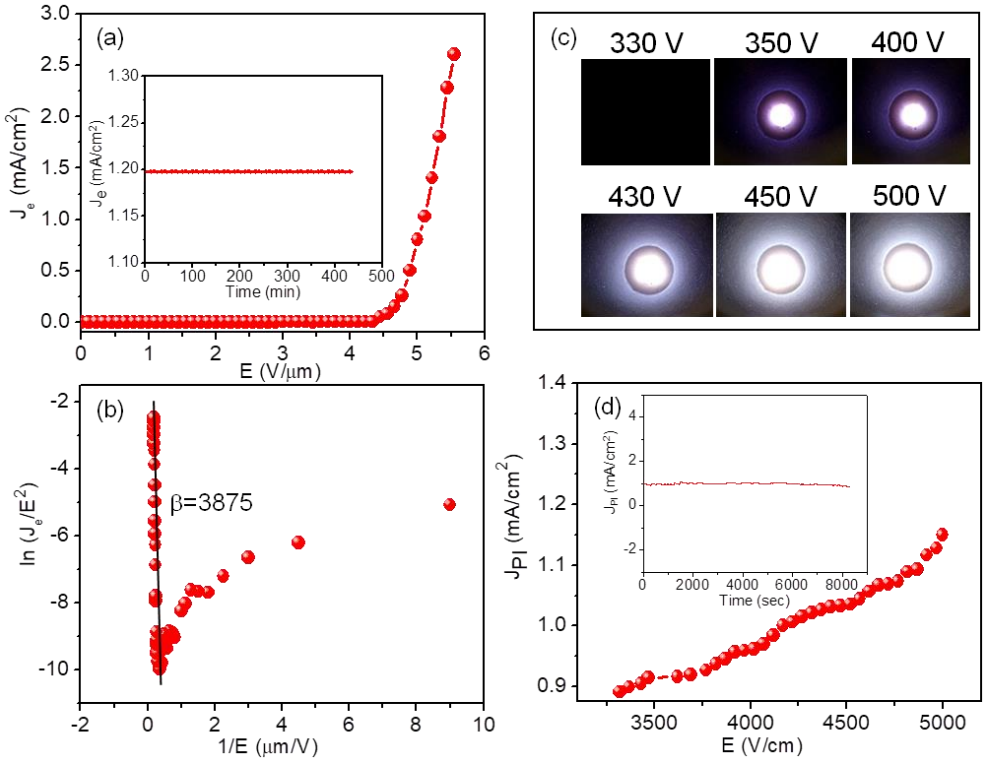

Figure. 9. Field electron emission (FEE) current density (J_e) as a function of the applied field (E) (a) and (b) the F-N plot corresponding to the J_e–E characteristic curve. The inset of (a) showing the FEE lifetime stability test, J_e versus time curve for D-ECNW nanostructures. (c) photographs of plasma illumination characteristics of the microplasma devices at varying applied voltages, and (d) the plasma current density versus applied field of a microplasma cavity. The inset of (d) shows the plasma illumination lifetime stability of these nanostructures.

3.5. Plasma illumination studies of diamond-enhanced carbon nanowalls

Recently, efficient FEE materials have become more predominant because of their potential for optoelectronic devices. Chiefly, microplasma-based devices possess a promising future regarding several applications, for example, the production of ozone, the detection of environmentally hazardous gases and vapors, display panels, and several biomedical and bioelectronics applications [67–69]. Numerous carbon-based materials such as carbon nanotubes, carbon nanowalls, graphene, etc. attain high emission of electrons and so are suitable as a cathode for these microplasma devices [70–73]. But, these cathode materials experience low lifetime stability [74–77] because the cathodes in the microplasma devices are subjected to continuous plasma ion bombardment during operation. For that reason, a material owning excellent robustness (long lifetime and reliability) and high secondary electron emission efficiency are necessary for acting as a cathode for these microplasma devices. Additionally, it

MOST WIEDZY Downloaded from mostwiedzy.pl

has been simulated that materials showing high FEE characteristics can markedly improve the performance of microplasma device characteristics [78,79].

Figure 9c shows the PI photographs of the microplasma devices, signifying that the D-ECNW nanostructures as a cathode ignited the plasma at a low voltage of 330 V corresponding to a threshold field of 0.33 V/μm. Also, the intensity of the PI photographs increases systematically with the applied voltage. Figure 9d indicates that the J_{PI} reaches a value of 1.2 mA/cm^{-2} at an applied field of 5000 V/cm (applied voltage=500 V). Furthermore, the PI lifetime stability of the D-ECNW nanostructures was inspected and it was found that the material can withstand more than 8348 s (139 min) under a tested current density of J_{PI}=1.0 mA/cm^2 (at E=4000 V/cm), which illustrates the high stability of these D-ECNW nanostructures. This performance of the D-ECNW nanostructures is much better than the microplasma devices which use other types of carbon emitters (carbon nanotubes, carbon nanowalls, and graphene nanowalls) as the cathode [74–77], which signifies that the diamond enhances the PI lifetime stability of these carbon nanowalls.

4. Conclusions

In summary, the combined effect of boron and nitrogen doping on the origin of edge-rich diamond-enhanced carbon nanowalls was investigated. These diamond-enhanced carbon nanowalls showed a hybrid nature comprising diamond-graphitic structure, in which boron species responsible for re-nucleation processes extending the length of the nanowalls, and the nitrogen doping induces the formation of graphene at the grain boundaries of the nanowalls. More conduction sites were observed at the surface of the nanowalls with a work function value of 4.75 eV. The peculiar structure of these edge-rich diamond-enhanced carbon nanowalls shows a noticeable enhancement in the field electron emission characteristics viz. a low turn-on field of 3.1 V/μm, a large field enhancement factor, a high FEE J_e of 2.6 mA/cm^{2,} and long lifetime stability of 438 min. The presence of graphene phases at the grain boundaries and sharp edges at the nanowall surfaces are the key factors for the enhancement of the field electron emission properties of these diamond-enhanced carbon nanowalls. The excellent performance with a low threshold voltage of 160 V and high plasma stability of 140 min of these diamond-enhanced carbon nanowalls as a cathode in a microplasma device paves the way for future plasma-based display applications.

MOST WIEDZY Downloaded from mostwiedzy.pl

Acknowledgments

The authors gratefully acknowledge financial support in part from the Polish National Science Centre (NCN) under Fast track COVID-19 grant No. 2020/01/0/ST7/00104 and the Foundation for Polish Science under the project Team-NET No. POIR.04.04.00-00-1644/1. The DS funds of the Faculty of Electronics, Telecommunications, and Informatics of the Gdańsk University of Technology are also acknowledged.

Conflict of Interest

The authors declare no competing financial interest.

Bibliography

[1] Y. Imai, K. Ueda, H. Itou, Y. Mizuno, H. Asano, in *2019 Compd. Semicond. Week CSW*, **2019**, pp. 1–1.
[2] A. Guerra, A. Achour, S. Vizireanu, G. Dinescu, S. Messaci, T. Hadjersi, R. Boukherroub, Y. Coffinier, J.-J. Pireaux, *Appl. Surf. Sci.* **2019**, *481*, 926.
[3] H. Nozaki, K. Takeda, M. Hiramatsu, **2018**, LW1.059.
[4] M. Hiramatsu, K. Shiji, H. Amano, M. Hori, *Appl. Phys. Lett.* **2004**, *84*, 4708.
[5] E. Luais, M. Boujtita, A. Gohier, A. Tailleur, S. Casimirius, M. A. Djouadi, A. Granier, P. Y. Tessier, *Appl. Phys. Lett.* **2009**, *95*, 014104.
[6] S. A. Evlashin, Y. M. Maksimov, P. V. Dyakonov, A. A. Pilevsky, K. I. Maslakov, Y. A. Mankelevich, E. N. Voronina, S. V. Vavilov, A. A. Pavlov, E. V. Zenova, I. S. Akhatov, N. V. Suetin, *Sci. Rep.* **2019**, *9*, 6716.
[7] K. J. Sankaran, M. Ficek, K. Panda, C.-J. Yeh, M. Sawczak, J. Ryl, K.-C. Leou, J. Y. Park, I.-N. Lin, R. Bogdanowicz, K. Haenen, *ACS Appl. Mater. Interfaces* **2019**, *11*, 48612.
[8] K. J. Sankaran, D. Q. Hoang, K. Srinivasu, S. Korneychuk, S. Turner, S. Drijkoningen, P. Pobedinskas, J. Verbeeck, K. C. Leou, I. N. Lin, K. Haenen, *Phys. Status Solidi A* **2016**, *213*, 2654.
[9] K. J. Sankaran, M. Ficek, K. Panda, C.-J. Yeh, M. Sawczak, J. Ryl, K.-C. Leou, J. Y. Park, I.-N. Lin, R. Bogdanowicz, K. Haenen, *ACS Appl. Mater. Interfaces* **2019**, *11*, 48612.
[10] K. J. Sankaran, M. Afsal, S.-C. Lou, H.-C. Chen, C. Chen, C.-Y. Lee, L.-J. Chen, N.-H. Tai, I.-N. Lin, *Small* **2014**, *10*, 179.
[11] D. Banerjee, K. J. Sankaran, S. Deshmukh, M. Ficek, G. Bhattacharya, J. Ryl, D. M. Phase, M. Gupta, R. Bogdanowicz, I.-N. Lin, A. Kanjilal, K. Haenen, S. S. Roy, *J. Phys. Chem. C* **2019**, *123*, 15458.
[12] R. Rani, K. Panda, N. Kumar, K. J. Sankaran, R. Pandian, M. Ficek, R. Bogdanowicz, K. Haenen, I.-N. Lin, *J. Phys. Chem. C* **2018**, *122*, 945.
[13] M. Pierpaoli, M. Ficek, M. Rycewicz, M. Sawczak, J. Karczewski, M. L. Ruello, R. Bogdanowicz, *Materials* **2019**, *12*, 547.
[14] K. Siuzdak, M. Ficek, M. Sobaszek, J. Ryl, M. Gnyba, P. Niedziałkowski, N. Malinowska, J. Karczewski, R. Bogdanowicz, *ACS Appl. Mater. Interfaces* **2017**, *9*, 12982.

MOST WIEDZY Downloaded from mostwiedzy.pl

[15] P. Niedziałkowski, Z. Cebula, N. Malinowska, W. Białobrzeska, M. Sobaszek, M. Ficek, R. Bogdanowicz, J. S. Anand, T. Ossowski, *Biosens. Bioelectron.* **2019**, *126*, 308.
[16] X. Zhou, Y. Zhang, J. Yang, J. Li, S. Luo, D. Wei, *Nanomaterials* **2019**, *9*, 496.
[17] H. Li, Y. Xiong, B. Wang, B. Yang, N. Huang, Y. Liu, J. Wen, *Diam. Relat. Mater.* **2018**, *87*, 228.
[18] P. Russo, M. Xiao, N. Y. Zhou, *Carbon* **2017**, *120*, 54.
[19] W. Wei, K. Sun, Y. H. Hu, *Ind. Eng. Chem. Res.* **2017**, *56*, 1803.
[20] S. Kamatchi Jothiramalingam, M. Ficek, S. Kunuku, K. Panda, C.-J. Yeh, J. Y. Park, M. Sawczak, P. P. Michalowski, K.-C. Leou, R. Bogdanowicz, I.-N. Lin, K. Haenen, *Nanoscale* **2018**, *10*, 1345.
[21] M. Hiramatsu, K. Shiji, H. Amano, M. Hori, *Appl. Phys. Lett.* **2004**, *84*, 4708.
[22] Y. Wu, P. Qiao, T. Chong, Z. Shen, *Adv. Mater.* **2002**, *14*, 64.
[23] M. Sobaszek, K. Siuzdak, J. Ryl, M. Sawczak, S. Gupta, S. B. Carrizosa, M. Ficek, B. Dec, K. Darowicki, R. Bogdanowicz, *J. Phys. Chem. C* **2017**, *121*, 20821.
[24] K. Siuzdak, M. Ficek, M. Sobaszek, J. Ryl, M. Gnyba, P. Niedziałkowski, N. Malinowska, J. Karczewski, R. Bogdanowicz, *ACS Appl. Mater. Interfaces* **2017**, *9*, 12982.
[25] Ch. Sommerhalter, Th. W. Matthes, Th. Glatzel, A. Jäger-Waldau, M. Ch. Lux-Steiner, *Appl. Phys. Lett.* **1999**, *75*, 286.
[26] S. Smidstrup, T. Markussen, P. Vancraeyveld, J. Wellendorff, J. Schneider, T. Gunst, B. Verstichel, D. Stradi, P. A. Khomyakov, U. G. Vej-Hansen, M.-E. Lee, S. T. Chill, F. Rasmussen, G. Penazzi, F. Corsetti, A. Ojanperä, K. Jensen, M. L. N. Palsgaard, U. Martinez, A. Blom, M. Brandbyge, K. Stokbro, *J. Phys. Condens. Matter* **2019**, *32*, 015901.
[27] J. Schneider, J. Hamaekers, S. T. Chill, S. Smidstrup, J. Bulin, R. Thesen, A. Blom, K. Stokbro, *Model. Simul. Mater. Sci. Eng.* **2017**, *25*, 085007.
[28] A. C. T. van Duin, S. Dasgupta, F. Lorant, W. A. Goddard, *J. Phys. Chem. A* **2001**, *105*, 9396.
[29] K. Stokbro, D. E. Petersen, S. Smidstrup, A. Blom, M. Ipsen, K. Kaasbjerg, *Phys. Rev. B* **2010**, *82*, 075420.
[30] B. Lukose, A. Kuc, J. Frenzel, T. Heine, *Beilstein J. Nanotechnol.* **2010**, *1*, 60.
[31] S. Smidstrup, D. Stradi, J. Wellendorff, P. A. Khomyakov, U. G. Vej-Hansen, M.-E. Lee, T. Ghosh, E. Jónsson, H. Jónsson, K. Stokbro, *Phys. Rev. B* **2017**, *96*, 195309.
[32] K. Jothiramalingam Sankaran, S. Kunuku, B. Sundaravel, P.-Y. Hsieh, H.-C. Chen, K.-C. Leou, N.-H. Tai, I.-N. Lin, *Nanoscale* **2015**, *7*, 4377.
[33] R. H. Fowler, L. Nordheim, *Proc. R. Soc. Lond. Ser. Contain. Pap. Math. Phys. Character* **1928**, *119*, 173.
[34] J. Ryl, A. Zielinski, L. Burczyk, R. Bogdanowicz, T. Ossowski, K. Darowicki, *Electrochimica Acta* **2017**, *242*, 268.
[35] N. Shang, P. Papakonstantinou, P. Wang, A. Zakharov, U. Palnitkar, I.-N. Lin, M. Chu, A. Stamboulis, *ACS Nano* **2009**, *3*, 1032.
[36] K. J. Sankaran, J. Kurian, H. C. Chen, C. L. Dong, C. Y. Lee, N. H. Tai, I. N. Lin, *J. Phys. Appl. Phys.* **2012**, *45*, 365303.
[37] Y. Wu, B. Yang, B. Zong, H. Sun, Z. Shen, Y. Feng, *J. Mater. Chem.* **2004**, *14*, 469.
[38] M. Hiramatsu, M. Hori, *Carbon Nanowalls: Synthesis and Emerging Applications*, Springer Science & Business Media, **2010**.
[39] R. Hawaldar, P. Merino, M. R. Correia, I. Bdikin, J. Grácio, J. Méndez, J. A. Martín-Gago, M. K. Singh, *Sci. Rep.* **2012**, *2*, 1.
[40] A. C. Ferrari, D. M. Basko, *Nat. Nanotechnol.* **2013**, *8*, 235.

MOST WIEDZY Downloaded from mostwiedzy.pl

[41] O. Frank, G. Tsoukleri, I. Riaz, K. Papagelis, J. Parthenios, A. C. Ferrari, A. K. Geim, K. S. Novoselov, C. Galiotis, *Nat. Commun.* **2011**, *2*, 1.
[42] T. M. G. Mohiuddin, A. Lombardo, R. R. Nair, A. Bonetti, G. Savini, R. Jalil, N. Bonini, D. M. Basko, C. Galiotis, N. Marzari, K. S. Novoselov, A. K. Geim, A. C. Ferrari, *Phys. Rev. B* **2009**, *79*, 205433.
[43] C. Androulidakis, E. N. Koukaras, J. Parthenios, G. Kalosakas, K. Papagelis, C. Galiotis, *Sci. Rep.* **2015**, *5*, 1.
[44] N. S. Mueller, S. Heeg, M. P. Alvarez, P. Kusch, S. Wasserroth, N. Clark, F. Schedin, J. Parthenios, K. Papagelis, C. Galiotis, M. Kalbáč, A. Vijayaraghavan, U. Huebner, R. Gorbachev, O. Frank, S. Reich, *2D Mater.* **2017**, *5*, 015016.
[45] P. Kovarik, E. B. D. Bourdon, R. H. Prince, *Phys. Rev. B* **1993**, *48*, 12123.
[46] S. Prawer, J. L. Peng, J. O. Orwa, J. C. McCallum, D. N. Jamieson, L. A. Bursill, *Phys. Rev. B* **2000**, *62*, R16360.
[47] J. Kurian, K. J. Sankaran, J. P. Thomas, N. H. Tai, H.-C. Chen, I.-N. Lin, *J. Phys. Appl. Phys.* **2014**, *47*, 415303.
[48] M. Sobaszek, K. Siuzdak, J. Ryl, M. Sawczak, S. Gupta, S. B. Carrizosa, M. Ficek, B. Dec, K. Darowicki, R. Bogdanowicz, *J. Phys. Chem. C* **2017**, *121*, 20821.
[49] O. A. Williams, M. Nesládek, *Phys. Status Solidi A* **2006**, *203*, 3375.
[50] K. J. Sankaran, K. Srinivasu, H. C. Chen, C. L. Dong, K. C. Leou, C. Y. Lee, N. H. Tai, I. N. Lin, *J. Appl. Phys.* **2013**, *114*, 054304.
[51] S. Kamatchi Jothiramalingam, M. Ficek, S. Kunuku, K. Panda, C.-J. Yeh, J. Y. Park, M. Sawczak, P. P. Michalowski, K.-C. Leou, R. Bogdanowicz, I.-N. Lin, K. Haenen, **2018**.
[52] R. L. Harniman, O. J. L. Fox, W. Janssen, S. Drijkoningen, K. Haenen, P. W. May, *Carbon* **2015**, *94*, 386.
[53] A. Vetushka, T. Itoh, Y. Nakanishi, A. Fejfar, S. Nonomura, M. Ledinský, J. Kočka, *J. Non-Cryst. Solids* **2012**, *358*, 2545.
[54] W. Takeuchi, H. Kondo, T. Obayashi, M. Hiramatsu, M. Hori, *Appl. Phys. Lett.* **2011**, *98*, 123107.
[55] V. Krivchenko, P. Shevnin, A. Pilevsky, A. Egorov, N. Suetin, V. Sen, S. Evlashin, A. Rakhimov, *J. Mater. Chem.* **2012**, *22*, 16458.
[56] P. Nath, S. Chowdhury, D. Sanyal, D. Jana, *Carbon* **2014**, *73*, 275.
[57] R. Gholizadeh, Y.-X. Yu, *J. Phys. Chem. C* **2014**, *118*, 28274.
[58] J. Rumble, Ed. , *CRC Handbook of Chemistry and Physics, 100th Edition*, **n.d.**
[59] T. Yuan, K. Larsson, *J. Phys. Chem. C* **2014**, *118*, 26061.
[60] S. Shen, W. Shen, S. Liu, H. Li, Y. Chen, H. Qi, *Mater. Today Commun.* **2020**, *23*, 100847.
[61] R. Sharma, S. Khan, V. Goyal, V. Sharma, K. S. Sharma, *FlatChem* **2017**, *1*, 20.
[62] R. Roy, A. Jha, D. Banerjee, N. Sankar Das, K. K. Chattopadhyay, *AIP Adv.* **2013**, *3*, 012115.
[63] H. Huang, Y. Li, Q. Li, B. Li, Z. Song, W. Huang, C. Zhao, H. Zhang, S. Wen, D. Carroll, G. Fang, *Nanoscale* **2014**, *6*, 8306.
[64] P.-H. Lin, C.-L. Sie, C.-A. Chen, H.-C. Chang, Y.-T. Shih, H.-Y. Chang, W.-J. Su, K.-Y. Lee, *Nanoscale Res. Lett.* **2015**, *10*, 297.
[65] V. I. Kleshch, D. A. Bandurin, A. S. Orekhov, S. T. Purcell, A. N. Obraztsov, *Appl. Surf. Sci.* **2015**, *357*, 1967.
[66] Y. Gao, S. Okada, *Carbon* **2020**, *157*, 33.
[67] K. (Ken) Ostrikov, U. Cvelbar, A. B. Murphy, *J. Phys. Appl. Phys.* **2011**, *44*, 174001.
[68] N. Barekzi, M. Laroussi, *Plasma Process. Polym.* **2013**, *10*, 1039.
[69] R. Sato, D. Yasumatsu, S. Kumagai, K. Takeda, M. Hori, M. Sasaki, *Sens. Actuators Phys.* **2014**, *215*, 144.

MOST WIEDZY Downloaded from mostwiedzy.pl

[70] M. W. Geis, N. N. Efremow, K. E. Krohn, J. C. Twichell, T. M. Lyszczarz, R. Kalish, J. A. Greer, M. D. Tabat, *Nature* **1998**, *393*, 431.
[71] M. Letizia Terranova, S. Orlanducci, M. Rossi, E. Tamburri, *Nanoscale* **2015**, *7*, 5094.
[72] J. Palomino, D. Varshney, O. Resto, B. R. Weiner, G. Morell, *ACS Appl. Mater. Interfaces* **2014**, *6*, 13815.
[73] A. Pandey, A. Prasad, J. P. Moscatello, Y. K. Yap, *ACS Nano* **2010**, *4*, 6760.
[74] T.-H. Chang, S. Kunuku, Y.-J. Hong, K.-C. Leou, T.-R. Yew, N.-H. Tai, I.-N. Lin, *ACS Appl. Mater. Interfaces* **2014**, *6*, 11589.
[75] K. Jothiramalingam Sankaran, T. Hsun Chang, S. Kumar Bikkarolla, S. Sinha Roy, P. Papakonstantinou, S. Drijkoningen, P. Pobedinskas, M. K. V. Bael, N.-H. Tai, I.-N. Lin, K. Haenen, *RSC Adv.* **2016**, *6*, 63178.
[76] K. J. Sankaran, K. Srinivasu, K. C. Leou, N. H. Tai, I. N. Lin, *Appl. Phys. Lett.* **2013**, *103*, 251601.
[77] K. J. Sankaran, C.-J. Yeh, S. Drijkoningen, P. Pobedinskas, M. K. Van Bael, K.-C. Leou, I.-N. Lin, K. Haenen, *Nanotechnology* **2017**, *28*, 065701.
[78] A. Venkattraman, A. Garg, D. Peroulis, A. A. Alexeenko, *Appl. Phys. Lett.* **2012**, *100*, 083503.
[79] A. Venkattraman, *Phys. Plasmas* **2015**, *22*, 057102.
[80] M. Hiramatsu, M. Hori, *Carbon Nanowalls: Synthesis and Emerging Applications*, Springer-Verlag, Wien, **2010**.

MOST WIEDZY Downloaded from mostwiedzy.pl